Nano Research
2023, 16(1): 439–448

ISSN 1998-0124 CN 11-5974/O4
https://doi.org/10.1007/s12274-022-4687-6

Research Article

Nano self-assembly of fluorophosphate cathode induced by surface energy evolution towards high-rate and stable sodium-ion batteries

Zhen-Yi Gu[1,§], Yong-Li Heng[1,§], Jin-Zhi Guo[1], Jun-Ming Cao[1], Xiao-Tong Wang[1], Xin-Xin Zhao[2], Zhong-Hui Sun[3], Shuo-Hang Zheng[1], Hao-Jie Liang[1], Bo Li[4] (✉), and Xing-Long Wu[1,2] (✉)

[1] *MOE Key Laboratory for UV Light-Emitting Materials and Technology, Northeast Normal University, Changchun 130024, China*
[2] *Department of Chemistry, Northeast Normal University, Changchun 130024, China*
[3] *Center for Advanced Analytical Science, School of Chemistry and Chemical Engineering, Guangzhou University, Guangzhou 510006, China*
[4] *Key Laboratory of Hazardous Chemicals Safety and Control Technology, School of Chemical and Environmental Engineering, North China Institute of Science and Technology, Langfang 065201, China*
[§] *Zhen-Yi Gu and Yong-Li Heng contributed equally to this work.*

Received: 9 April 2022 / **Revised:** 11 June 2022 / **Accepted:** 21 June 2022

ABSTRACT

In the field of materials science and engineering, controlling over shape and crystal orientation remains a tremendous challenge. Herein, we realize a nano self-assembly morphology adjustment of $Na_3V_2(PO_4)_2F_3$ (NVPF) material, based on surface energy evolution by partially replacing V^{3+} with aliovalent Mn^{2+}. Crystal growth direction and surface energy evolution, main factors in inducing the nano self-assembly of NVPF with different shapes and sizes, are revealed by high-resolution transmission electron microscope combined with density functional theory. Furthermore, NVPF with a two-dimensional nanosheet structure (NVPF-NS) exhibits the best rate capability with 68 mAh·g^{-1} of specific capacity at an ultrahigh rate of 20 C and cycle stability with 80.7% of capacity retention over 1,000 cycles at 1 C. More significantly, when matched with Se@reduced graphene oxide (rGO) anode, NVPF-NS//Se@rGO sodium-ion full cells display a remarkable long-term stability with a high capacity retention of 93.8% after 500 cycles at 0.5 C and −25 °C. Consequently, experimental and theoretical calculation results manifest that NVPF-NS demonstrates such superior performances, which can be mainly due to its inherent crystal structure and preferential orientation growth of {001} facets. This work will promise insights into developing novel architectural design strategies for high-performance cathode materials in advanced sodium-ion batteries.

KEYWORDS

nano self-assembly, sodium-ion batteries, cathode, fluorophosphate

1 Introduction

In the past several decades, sodium-ion batteries (SIBs) have drawn wide interest on account of their prominent electrochemical performances, low cost, and abundant sodium sources [1–3]. Nevertheless, large ion radius of 1.02 tends to restrict Na^+ from intercalating into/extracting from the host materials, thus leading to insufficient electrochemical performances for SIBs and hard to practical application [4–7]. As a result, it is fundamental to exploit and optimize various cathode materials with ultra-stable structure, appropriate morphology, as well as satisfactory energy density for high-performance SIBs [8–13]. At present, cathode materials mainly include layered transition metal oxides [14–22] (e.g. Na_xTMO_2, TM = Mn, Fe, Co, Ni, etc.), polyanion-type compounds [23–28] (e.g. $Na_3V_2(PO_4)_3$, $Na_4MnV(PO_4)_3$, $Na_3V_2(PO_4)_2F_3$), and Prussian blue analogs [29–32] (e.g. $Na_2M[Fe(CN)_6]$, M = Fe, Co, Mn, Ni, etc.). Among these reported cathode materials, $Na_3V_2(PO_4)_2F_3$ (NVPF) has been considered as a promising candidate by virtue of its stable crystal structure, extraordinary average working voltage (3.9 V vs. Na^+/Na), and theoretical specific capacity (C_s) (128 mAh·g^{-1}) [33]. But unfortunately, many studies show that pristine NVPF in fact still suffers from unsatisfactory practical discharge C_s and cycling performance, which may be hindered mainly by its very poor intrinsic electronic conductivity (10^{-12} S·cm^{-1}) [34, 35].

Currently, most research strategies on NVPF are usually through the construction of conductive carbon coatings [24, 34, 36] and element doping [37–41] to ameliorate the electronic conductivity of NVPF and reduce side reactions between electrode materials and electrolytes, so as to achieve the enhanced electrochemical performances of NVPF. However, unremitting efforts are still needed to boost rate capability and cycling performance for advanced SIBs. Generally, controlling morphology and size of sample particles plays a significant role in improving charge transfer dynamics, structural and electrochemical stability, as well as interfacial compatibility between electrode material and electrolyte [42–45]. So far, a certain amount of studies have been done on the electrochemical enhancement brought about by the shape of material itself and the particle growth process [46–51]. Learning from previous research, it is found that nanostructures are equipped with a shorter diameter and a larger specific surface area, which are capable of

Address correspondence to Bo Li, libo@ncist.edu.cn; Xing-Long Wu, xinglong@nenu.edu.cn

reducing the diffusion path of electrons and ions while increasing the amount of active sites in electrode materials, thereby promoting rate and cycling capability [35]. Among a series of microstructures such as zero dimensional (0D) nanospheres, 1D nanofibers, 2D nanosheets, and 3D porous architectures, active materials with the 2D nanosheet structure generally prefer to exhibit both amazing rate performance and long-term life owing to its unique advantages of numerous active sites and shorted ion transport paths. Unfortunately, it is difficult to rationally control size and morphology for cathode materials due to their complex components, especially for NVPF. In accordance with previous reports, researchers have used surfactant-assisted or pH-regulative strategies to achieve the suitable size and morphology control for NVPF. For example, Criado et al. used oleic acid as a surfactant to obtain an ideal morphology with a high evenly distribution and embedded into carbon networks [52]. Also, Li et al. found that SPAN 80, stearic acid, and octadecyl amine were applied as three different surfactant molecules to construct NVPF materials with nanoflakes, nanorods, and nanocubes structures, separately [36]. Besides, Dai's group indicated that NVPF nanoflowers can be synthesized by pH-regulation [53]. However, as far as we are aware, there has been no literature on the nano self-assembly adjustment of NVPF by means of using aliovalent ions to modulate V sites.

Herein, a series of NVPF samples with various shapes and sizes were successfully prepared by using aliovalent Mn^{2+} to adjust the V positions in NVPF. Moreover, with increase of the amount of aliovalent Mn^{2+}, NVPF material can realize a precisely controlled morphology adjustment from the randomly distributed microtetraprisms (NVPF-MTP) at the beginning and gradually self-assemble into regular 2D nanosheets (NVPF-NS), then 3D microballs (NVPF-MB), sub-microballs (NVPF-SMB), and finally nanoparticles (NVPF-NP). The calculation results according to density functional theory (DFT) demonstrate that introduction of aliovalent Mn^{2+} can contribute to surface energy evolution of NVPF materials and hence induce NVPF to self-assemble into different microstructures. In particular, when applied as cathode material for SIBs, NVPF-NS exhibits the optimal electrochemical properties, which is largely attributed to Mn^{2+} substitution into NVPF crystal lattice leading to the coexistence of V^{3+} with V^{4+}, and thus enhancing electronic conductivity and structural stability of NVPF. At the same time, aliovalent Mn^{2+} regulates the crystal lattice and surface energy of the material to self-assemble into a unique 2D nanosheet structure, which shortens Na^+ migration path and promotes ion transport in the NVPF-NS material, bringing about an increased Na^+ diffusion rate in the crystal lattice. Additionally, both performance improvement and internal mechanism on the basis of aliovalent Mn^{2+} induced NVPF lattice adjustment to achieve the self-assembled 2D nanosheet structure are investigated adequately with the help of scanning electron microscopy (SEM), cyclic voltammetry (CV), galvanostatic intermittent titration technique (GITT), *in-situ* X-ray diffraction (XRD), and first-principles DFT calculations. Moreover, NVPF-NS also presents superior low-temperature (LT) performance, which has access to a C_s of ~ 95 mAh·g^{-1} even at −25 °C and obtains a capacity retention of over 95% after 350 cycles. More surprisingly, excellent rate capability and long-term cycling stability can be achieved for sodium-ion full cells (SIFCs) when matched with Se@reduced graphene oxide (rGO) anode. Particularly, a capacity retention up to 93.8% can be accomplished over 500 cycles at 0.5 C and −25 °C. This study has demonstrated convincingly that crystal lattice of fluorophosphate can be effectively controlled to realize the nano self-assembly of the material with a 2D nanosheet structure based on aliovalent substitution, thus improving the stability of crystal structure and realizing an outstanding energy storage capability in half and full cells for great application prospects.

2 Results and discussion

XRD patterns were employed to identify the crystal structure of our prepared NVPF-MTP, NVPF-NS, NVPF-MB, NVPF-SMB, and NVPF-NP samples. As shown in Fig. S1 in the Electronic Supplementary Material (ESM), they have a number of diffraction peaks that can be fully indexed to $Na_3V_2(PO_4)_2F_3$ (JCPDS NO. 89-8945) with $P4_2/mnm$ space group belonging to tetragonal crystal system. Moreover, all observed diffraction peaks are sharp and intense, indicating the high crystallinity. At the same time, no impurity peaks were detected, confirming the high purity of these prepared materials. An appropriate amount of Mn^{2+} doping did not damage the integrity of NVPF crystal structure. Also, Le Bail refinement of the prepared NVPF-NS material is displayed in Fig. 1(a) with the cell parameters of $a = b = 9.0394(5)$, $c = 10.6189(6)$ (Table S1 in the ESM). Based on XRD data and Le Bail refinement, the schematic illustration of NVPF-NS crystal lattice was showed, where $[V_2O_8F_3]$ bi-octahedra units and $[PO_4]$ tetrahedra units constructed a 3D open framework, while doping Mn^{2+} (with a larger ionic radius of 0.97 Å compared to that of 0.78 Å for V^{3+}) occupied part of V sites, accounting for vast transport paths for Na^+ (Fig. 1(b)). Fourier transform infrared spectrum (FTIR) investigation was further conducted to obtain detailed information about bonding modes of the atoms in NVPF-NS material. As shown in Fig. S2 in the ESM, a typical broad band appearing at the range from 1,200 to 1,000 cm^{-1} is designated to the asymmetrical stretching vibration of PO_4^{3-} unit, while a strong peak locating at 921 cm^{-1} can be identified as the vibration of V–O bond. Peaks at 672 and 556 cm^{-1} can be considered as the symmetrical stretching vibration and the bending vibration of P–O bond, respectively.

Figure 1(c) is the selected area electron diffraction (SAED), which is applied to identify the direction of crystal growth [54–56]. SAED patterns were analyzed to imply the internal mechanism of morphological transformation for above mentioned unique 2D nanosheet from the perspective of crystal structure. As shown in Fig. 1(c), it can be speculated that nanoparticles grow preferentially along the [001] direction to self-assemble into a unique 2D nanosheet structure finally. Transmission electron microscopy (TEM) image and SEM test of as-prepared NVPF-NS sample were employed to obtain its microscopic morphology and the results are shown in Fig. 1(d) and Fig. S3 in the ESM. It is found that a distinct 2D nanosheet structure with an average size of 1–2 μm and a sheet thickness of ~ 0.1 μm can be observed clearly. Simultaneously, it should be pointed out that this unique morphology is different from those typically reported in Refs. [34, 52, 57, 58]. Also, there is a uniform element distribution of Na, V, Mn, C, O, P, and F in the sample from the energy dispersive spectroscopy (EDS) mapping results, as shown in Fig. 1(e). In order to confirm Mn^{2+} has been successfully introduced into NVPF lattice, high-resolution X-ray photoelectron spectroscopy (XPS) and inductively coupled plasma-atomic emission spectroscopy (ICP-AES) tests were conducted. According to the deconvolution results from high-resolution XPS in Fig. 1(f), there are a couple of additional peaks representing V^{4+} (523.13 and 516.59 eV) in NVPF-NS. In addition, V^{3+}:V^{4+} = 3.21 was obtained by XPS peak fitting, which means that the presence of V^{4+} is induced by the generation of crystal defects after the substitution of aliovalent Mn^{2+} at the V site. Also, they both delivered an additional Mn-induced peak, which can be classified as the deconvoluted Mn–O and Mn–F from O 1s and F 1s spectra (Figs. 1(g) and 1(h)), separately. All the results indicate that Mn^{2+}

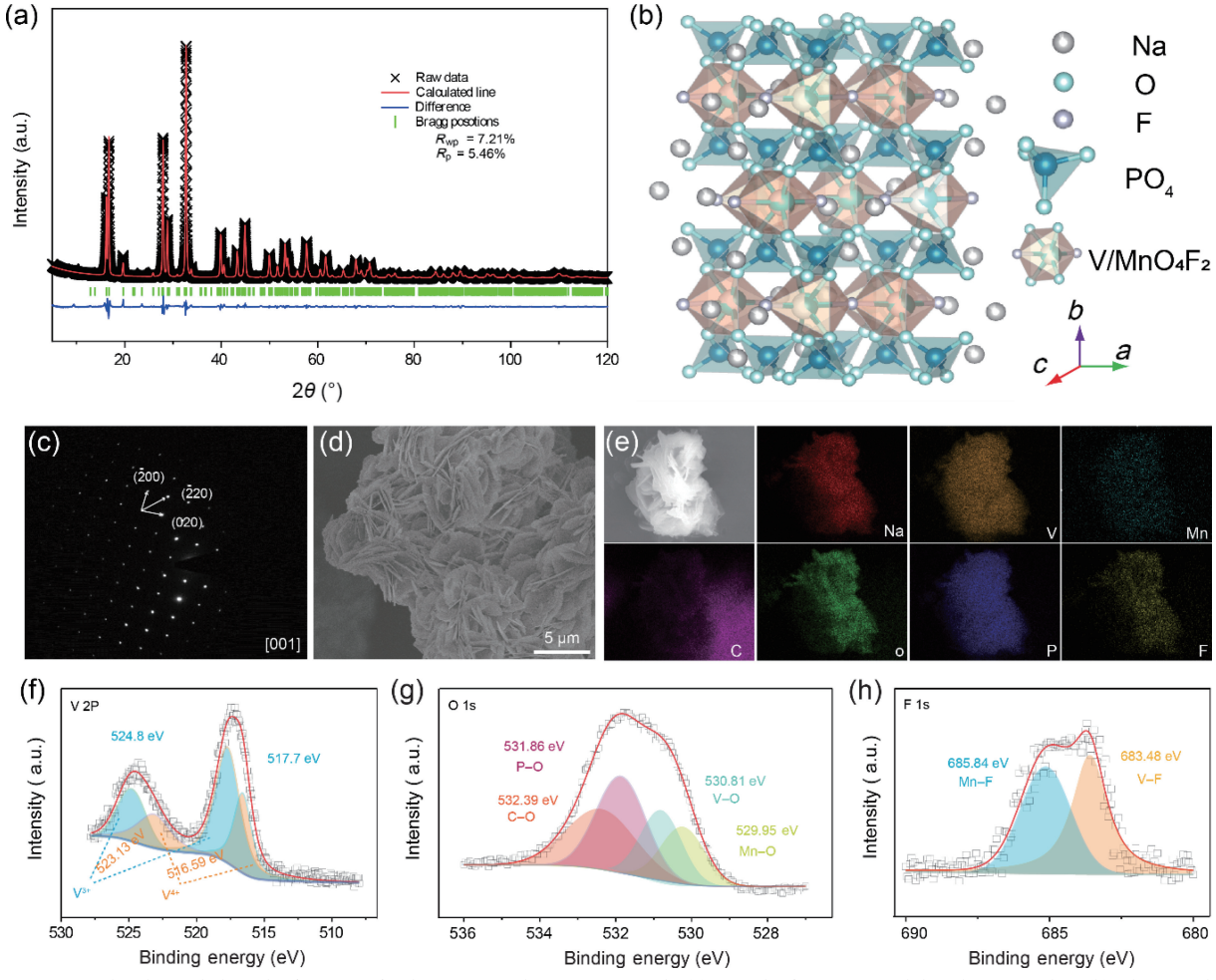

Figure 1 Structural and morphological information for the as-prepared NVPF-NS sample: (a) Le Bail refinements result based on XRD data; (b) schematic diagram of NVPF-NS crystal structure; (c) SAED pattern; (d) SEM image; (e) EDS mapping; high-resolution XPS spectra of (f) V 2p, (g) O 1s, and (h) F 1s.

has been successfully introduced into NVPF lattice and strongly interacts with O and F atoms. In addition, the aliovalent Mn^{2+} partially replaces V in NVPF and thus induces V sites to produce defects, resulting in the mixed existence of V^{3+}/V^{4+}, which will be beneficial to improving the electronic conductivity of NVPF. According to ICP-AES tests (Table S2 in the ESM), the molar ratio of Na, V, and Mn elements conforms to the findings obtained from EDS mapping and full XPS spectra. In addition, the full XPS spectra also clearly confirms the coexistence of Na, V, Mn, C, O, P, and F in the NVPF-NS sample, as presented in Fig. S4 in the ESM.

Surprisingly, our study has signified that surface morphology can be regulated with the increasing Mn content in the samples. Figure 2(a) is schematic illustration of morphology control for NVPF by Mn^{2+} substitution. Firstly, the original NVPF without Mn^{2+} substitution shows a number of randomly distributed microtetraprisms. And then the microtetraprism structure evolves into a distinctive 2D sheet structure when the molar ratio of doped Mn to V is exactly equal to 0.1 over 1.9 (x = 0.1). Subsequently, the microstructure in turn transforms into 3D porous microball structure as more Mn^{2+} goes into the crystal lattice for $Na_{3+x}V_{2-x}Mn_x(PO_4)_2F_3$ (x = 0.3). Furthermore, it returns to 3D sub-microball structure formed by stacked cubes and followed by nanoparticles when introducing more Mn sources into the samples (x = 0.5 and 0.7). The above discussion can be strongly substantiated in terms of SEM images for the five representative NVPF-MTP, NVPF-NS, NVPF-MB, NVPF-SMB, NVPF-NP samples, which are able to capture their morphological features directly. As shown in Fig. S5(a) in the ESM, the pristine NVPF without Mn source addition generally appears a typical tetraprism shape with the average size of ~ 3 μm × 2 μm × 1 μm. In the beginning, along with the addition of Mn to reach a certain molar ratio (Mn:V = 0.1:1.9), initial morphology disappears completely and transforms into another distinct morphology made of stacked 2D nanosheet structure, which is conducive to giving full play to the electrochemical properties of NVPF material. As displayed in Fig. S5(b) in the ESM, it can be observed clearly that these smooth nanosheets have an average size close to 2 μm with a thickness of ~ 0.1 μm. Sequentially, when continuing to add the Mn source until the molar ratio of Mn to V is equal to 0.3 to 1.7 (Fig. S5(c) in the ESM), 2D nanosheet structure also vanishes and instead a number of small nanocubes primary particles (about 200 nm) aggregating into typical secondary microspheres with the average diameter of 1.5–2 μm come out. Subsequently, a slightly smaller average diameter of ~ 1 μm of these sub-microballs has been evidenced in Fig. S5(d) in the ESM when the molar ratio of Mn to V increases to 0.5:1.5. At last, the regular morphology is damaged and transforms into obviously fewer regular nanoparticles with the ratio of Mn to V increasing to 0.7:1.3 (in Fig. S5(e) in the ESM), which may be due to introducing a great amount of Mn^{2+} with a larger ionic radius into crystal lattice, thus leading to the collapse of gross morphologies. As a result, it can be summed up that NVPF goes through an unprecedented self-assembly adjustment from irregular bulks to a series of morphological changes of 2D nanosheets and microballs as the amount of aliovalent Mn^{2+} instead of V^{3+} into the crystal lattice increases. This means that the content of aliovalent Mn^{2+} is a decisive factor in inducing NVPF to self-assemble into different structures.

Although an interesting phenomenon about morphology

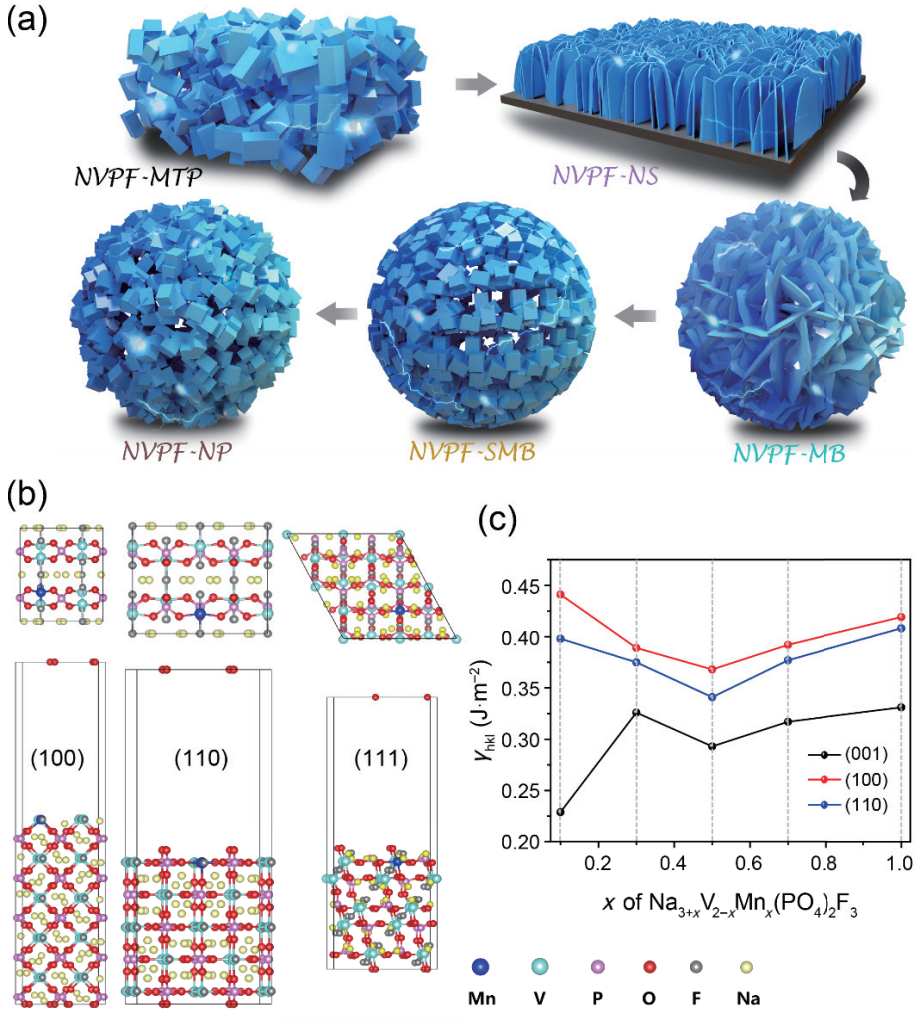

Figure 2 (a) Schematic diagram of morphology evolution process for NVPF-MTP, NVPF-NS, NVPF-MB, NVPF-SMB, and NVPF-NP samples by the substitution of V^{3+} with different Mn^{2+} concentrations. Theoretical calculation: (b) calculated ball-and-stick model of $Na_{3+x}V_{2-x}Mn_x(PO_4)_2F_3$ (x = 0.1, 0.3, 0.5, 0.7, and 1) samples: top view (top) and side view (bottom) of (100), (110), and (111) facets. Color code for different elements: Mn in blue, V in indigo, P in pink, O in red, F in grey, and Na in yellow. (c) Surface energy evolution of three representative crystal facets of (001), (100), and (110) with different Mn concentrations.

evolution has been uncovered, the internal mechanism still needs to be further explored. In order to grasp more insights into the underlying mechanism of morphology control for NVPF, the first-principles calculations based on DFT were performed. Specifically, the calculated results of surface energies for some typical crystal faces are shown in Figs. 2(b) and 2(c). It is well defined that surface energy can reveal the stability of the corresponding plane, thus affecting the crystal growth and morphology [59, 60]. In generally, surface energy values of different crystal faces are different in a selected crystal. For example, it can be obviously seen that surface energy γ_{hkl} of (001) facet for $Na_{3+x}V_{2-x}Mn_x(PO_4)_2F_3$ (x = 0.1) is much lower than that of (100) and (110) facets, indicating that (001) facet is more stable than (100) and (110) facets and hence the growth rate of (001) facet is slower than that of (100) and (110) facets. As a consequence, $Na_{3+x}V_{2-x}Mn_x(PO_4)_2F_3$ (x = 0.1) crystal grows preferentially along the axial direction of (001) crystal plane to form a 2D sheet architecture, as shown in Fig. S5(b) in the ESM by SEM tests. On the other hand, as for other $Na_{3+x}V_{2-x}Mn_x(PO_4)_2F_3$ (x = 0.3, 0.5, 0.7, and 1) samples, their surface energies of (001) facet increase significantly compared to the initial sample. Although they are still slightly lower than those of (100) and (110) facets, the differences among these surface energy values for three crystal facets become relatively smaller. Maybe that explains why these samples are composed of numerous 3D cubic primary particles. In short, the results based on theoretical calculation are also well agreement with the aforementioned SAED and SEM images.

Galvanostatic charge/discharge (GCD) curves were applied to probe into the effects of Mn^{2+}-induced different morphologies on the enhancement of electrochemical performances. At first, Fig. 3(a) characterizes the representative GCD curves for NVPF-MTP, NVPF-NS, NVPF-MB, NVPF-SMB, and NVPF-NP electrodes from 2.0 to 4.3 V (vs. Na^+/Na) at 0.1 C (1 C = 121.6 mA·g^{-1}). In sharp contrast to the four NVPF-MTP, NVPF-MB, NVPF-SMB, and NVPF-NP electrodes, NVPF-NS electrode can deliver the highest reversible C_s of ~ 118 mAh·g^{-1} with a highest coulombic efficiency (E_c) of 84.2%, indicating that the crystal structure of NVPF-NS possesses the optimal reversibility to withstand the de-/embedding of two Na^+. However, compared with NVPF and other materials, the initial coulombic efficiencies of all materials are lower than 90%, which is mainly attributed to the formation of cathode electrolyte interface (CEI) and partial electrolyte decomposition [37]. In addition, two noticeable pairs of charge/discharge plateaus for all the electrodes can be observed at about 4.03/4.00 V and 3.64/3.60 V, which are mainly attributed to V^{3+}/V^{4+} redox couples along with Na^+ extraction from/insertion into NVPF host materials. The above results are also in good agreement with the previous Refs. [61–63]. As well as it can be seen from GCD curve that there is a negligible polarization during charge–discharge process, elucidating NVPF-NS experiences a

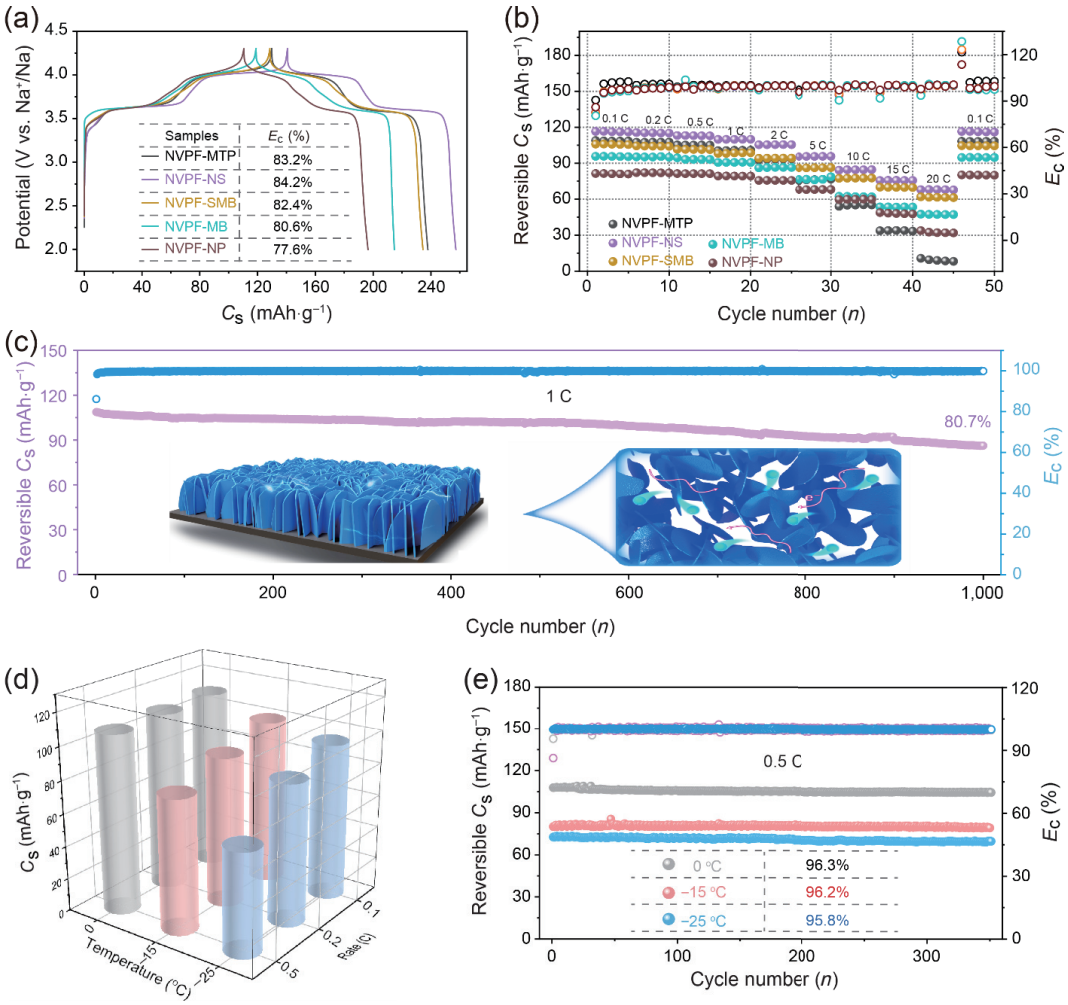

Figure 3 Electrochemical performances of sodium-ion half cells with NVPF-MTP, NVPF-NS, NVPF-MB, NVPF-SMB, and NVPF-NP electrodes within the voltage window of 2.0–4.3 V vs. Na^+/Na: (a) GCD curves and inset is their corresponding E_c; (b) rate capability; (c) cyclic performance at 1 C for NVPF-NS and specific transport paths of electron and Na^+ are displayed by inset of (c); (d) 3D columnar diagram of rate capability and (e) cycling performance in the low temperatures with corresponding capacity retentions (inset) for NVPF-NS.

highly reversible ion-(de)intercalation process accompanied by reduced charge transfer resistance and improved electronic conductivity. Figure 3(b) displays the rate capability at a series of different current densities of the as-prepared five NVPF electrodes. As a comparison of pristine NVPF-MTP, capacity attenuation is apparently suppressed for those NVPF samples with Mn substitution. It can be seen that the highest discharge C_s of 116, 115, 113, 110, 105, 96, 85, 76, and 68 mAh·g^{-1} is obtained for NVPF-NS at increasing rates of 0.1, 0.2, 0.5, 1, 2, 5, 10, 15, and 20 C, separately. Also, when the rate gets back to initial 0.1 C, its C_s will also recover to approach the initial value. Figure S6 in the ESM shows GCD curves under various rates from 0.1 to 20 C. Particularly, GCD curve still shows two obvious pairs of charging and discharging plateaus even under the ultrahigh rate of 20 C, maintaining a good curve profile. This signifies that NVPF-NS has not only excellent structural stability but also fast Na^+ migration rate. The superior rate capability is probably because of the synergistic effects of Mn^{2+} substitution and unique 2D nanosheet structure, which are capable of providing a large number of active sites and shortening Na^+ transport paths. Cycling performances were also examined in Fig. 3(c). It is worth mentioning that the NVPF-NS sample still delivers 80.7% of capacity retention over 1,000 cycles at 1 C. At the same time, no particle agglomeration and cracks appeared in the cycled NVPF-NS electrode according to the SEM and TEM images (Fig. S7 in the ESM). Furthermore, the E_c remains close to 100% during the cycle, which is mainly due to the fact that substitution of Mn^{2+} enhances the stability of NVPF crystal structure and the unique 2D nanosheet structure improves the overall cycle stability of the material by alleviating severe volume changes during the Na^+-(de)intercalation process, as presented in the inset of Fig. 3(c). The outstanding electrochemical performances in the low temperatures were also evaluated for sodium-ion half cells.

In addition, we performed electrochemical tests along with the operation temperature ranging from 0 to −25 °C. As shown in Fig. 3(d), NVPF-NS cathode delivers a highly promising C_s of about 95 mAh·g^{-1} at 0.1 C and −25 °C, implying superior LT performance of NVPF-NS cathode. It is exciting that NVPF-NS cathode owns the superior cycling performance with an extraordinary capacity retention exceeding 95% obtained in different temperatures for 350 cycles at 0.5 C, implying that Mn^{2+}-introduction has strengthened the stability of crystal structure for NVPF cathode (Fig. 3(e)). Given the above electrochemical test results, it can be concluded that NVPF-NS material, which is self-assembled into 2D nanosheets after the substitution of aliovalent Mn^{2+}, has outstanding rate, cycle performance, and excellent LT performance when used as SIBs positive electrode. This may be mainly on account of the fact that aliovalent Mn^{2+} enhances the lattice stability of NVPF and unique 2D nanosheet structure accelerates Na^+ migration rate and enhances structural stability.

In consideration of the important influence of Mn^{2+} introduction on the kinetics of NVPF materials, CV (Figs. 4(a) and 4(b)) and GITT (Fig. 4(c)) tests were conducted to further study Na^+ migration kinetics of NVPF-NS cathode. To gain a

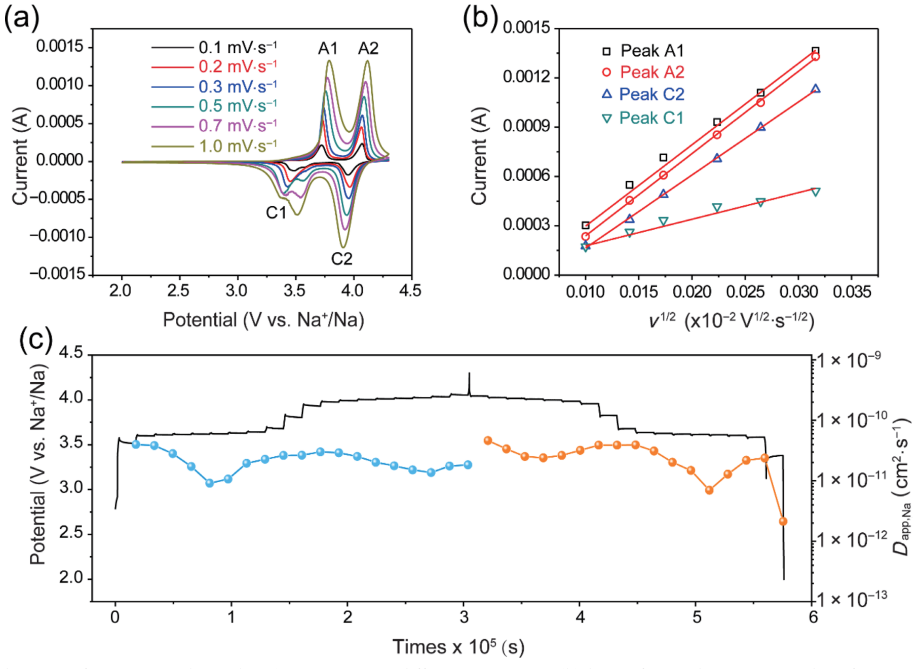

Figure 4 Na^+ migration kinetics of NVPF-NS electrode: (a) CV curves at different scan rates; (b) linear fittings between i_p and $v^{1/2}$ from CV curves; (c) GITT results with the evolutions of $D_{app, Na}$ and quasiequilibrium potential during the charging–discharging cycle.

better understanding of computation process for apparent Na^+ diffusion coefficient ($D_{app, Na}$), the readers are advised to note the relevant detailed explanations (as shown in the ESM). Figure 4(a) displays CV tests at various scan rates. Obviously, redox peak current (i_p) also increases and potential difference value between each redox couple becomes augmented slightly in the scan rate ranging from 0.1 to 1.0 $mV·s^{-1}$. Nevertheless, the shapes of curves remain almost the same, demonstrating high reversibility of the correlative redox reactions. Moreover, the presence of PC and FEC in the SIBs electrolyte solution leads to the formation of a passivation layer on the surface of metallic sodium, and the increased polarization in the low-voltage region results in a split reduction peak at 3.5 V [64]. In addition, remarkable linear fittings between i_p and square root of scan rates ($v^{1/2}$) manifest that the electrochemical behaviors of NVPF-NS are dominated by Na^+ diffusion process [65] (as shown in Fig. 4(b)). Besides, $D_{app, Na}$ values assigned to each redox peak from stepwise Na^+ insertion/extraction can be calculated based on Randles–Sevcik equation [66]. Manifestly, NVPF-NS electrode possesses higher $D_{app, Na}$ values than other phosphate cathode materials (Fig. 4), implying the redox reactions occur accompanied by accelerated apparent Na^+ diffusion kinetics.

Additionally, GITT profiles disclose the evolution of $D_{app, Na}$ for NVPF-NS cathode throughout the charging and discharging process (Fig. S8 in the ESM and Fig. 4(c)). NVPF-NS shows a higher $D_{app, Na}$ in a narrow range of about 10^{-9}–10^{-11} $cm^2·s^{-1}$ and the fluctuation of $D_{app, Na}$ value is smaller than that of reported NVPF materials (about 10^{-9}–10^{-13} $cm^2·s^{-1}$) [4, 34]. Smaller $D_{app, Na}$ fluctuations mean that NVPF-NS material is relatively easy for Na^+ (de)intercalation during the (dis)charging process. In addition, NVPF-NS has faster Na^+ migration rate in the plateaus area. Compared with other NVPF materials that have been reported [41, 45], rapid migration in the plateaus area will be more conducive to the rate performance. CV and GITT results insinuate that Mn^{2+} is introduced into NVPF lattice, which thus produces a unique 2D nanosheet structure, and thereby the electrode kinetics are enhanced. From the perspective of these results obtained above, lattice regulation of NVPF based on V^{3+}-substitution with aliovalent Mn^{2+} is proven to be able to not only increase electronic conductivity of active material by creating crystal defects, thereby reducing battery polarization, but also induce NVPF to self-assemble into unique 2D nanosheets with improved Na^+ diffusion rate. These should be crucially responsible for the enhanced rate capability and sodium storage performances for NVPF-NS material.

In order to uncover the mechanism of Na^+ intercalation/extraction, structural evolution of NVPF-NS was represented by *in-situ* XRD collected every 15 min at 0.5 C during the first GCD cycle. The high reversibility from the perspective of peak intensity and angle originated from NVPF-NS crystal planes during the whole cycle is illustrated by full-scale *in-situ* XRD in 2D color mode, which was conducted from 15° to 35° (Fig. 5(a)). Also, the selective *in-situ* XRD curves of 2θ angle (15°–35°) with strong diffraction peaks from (220), (113), and (222) planes are displayed to study the Na^+ insertion/extraction process by monitoring peak shifts (Fig. 5(b)). During the initial charging process (the first Na^+ extraction occurring at approximately 3.6 V, as displayed in Fig. 5(c)), two peaks locating at ~ 28.07° and 32.87° are identified from (220) and (222) planes, separately, which tend

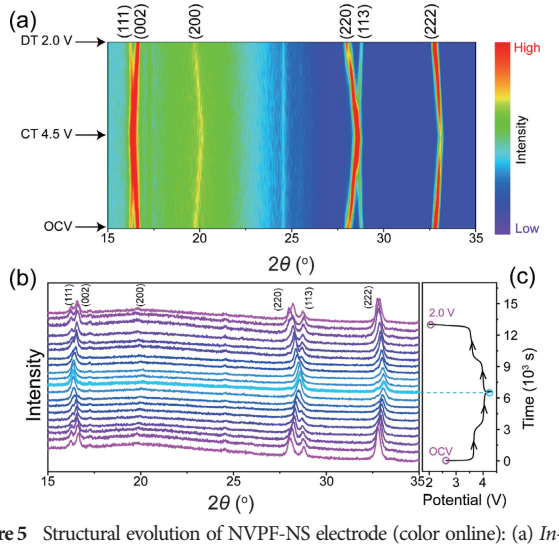

Figure 5 Structural evolution of NVPF-NS electrode (color online): (a) *In-situ* XRD in 2D color format and (b) selective *in-situ* XRD curves from 15° to 35°; (c) the corresponding GCD curve.

to shift to higher angles. These peak variations correspond to a phase transition from $Na_3V_2(PO_4)_2F_3$ to the conductive $Na_2V_2(PO_4)_2F_3$. When continuing to charge until the cut-off voltage is 4.3 V, the diffraction peak angle from (220) plane further offsets to a larger value and then consolidates with an adjacent peak of (113) plane to form a broad diffraction peak, while the peak at 33.06° also moves to a higher angle, suggesting the transformation from $Na_2V_2(PO_4)_2F_3$ to $NaV_2(PO_4)_2F_3$ accompanied by the second Na^+ extraction. Afterwards, when discharging to 2.0 V, all diffraction peaks can be well recovered to their pristine states, which proves NVPF-NS goes through a highly reversible crystal structure evolution ($Na_3V_2(PO_4)_2F_3 \leftrightarrow NaV_2(PO_4)_2F_3 + 2Na^+ + 2e^-$) during Na^+ insertion/extraction processes.

Furthermore, inspired by the outstanding electrochemical and dynamic properties for sodium-ion half cells, the comprehensive electrochemical performances were also evaluated in the assembled SIFCs coupled with NVPF-NS cathode and Se@rGO anode (Fig. 6(a)). It is worth pointing out that the Se@rGO anode used here was prepared like our previous work [67]. Firstly, the SIFCs demonstrate outstanding energy storage application prospects in consideration of rate capability and long-term stability at 25 °C. As demonstrated in Fig. 6(b), rate capability is performed ranging from 0.1 to 20 C, and the discharge C_s can still reach 85.7 mAh·g^{-1} even at an exceedingly high rate of 20 C (71.4% of C_s at 0.1 C). Moreover, compared with the half cells, the initial E_c of NVPF-NS//Se@rGO SIFCs is lower, which is mainly due to the fact that the full cells will undergo the activation process during the first cycle [68, 69]. It is surprising that NVPF-NS//Se@rGO SIFCs deliver the obviously improved rate performance compared to the corresponding data from half-cell tests especially at the high rates (Fig. 6(b)), which should be due to the extra side reactions of Na metal electrode in the half cells. Normally, in half cells, Na metal electrode inevitably forms Na dendrites during the deposition/dissolution process accompanied by continuous consumption of electrolyte, severe volumetric change, and the formation of unstable solid electrolyte interphase, especially at high current density, which may severely impact the electrochemical performance of half cells [70, 71]. In addition, the SIFCs exhibit superior cycling performance with 90.4% of capacity retention at 0.5 C after 300 cycles (Fig. 6(c)). Meanwhile, the electrochemical performance tests were also performed at the low temperatures for SIFCs. The excellent rate capability of NVPF-NS//Se@rGO SIFCs is testified in Fig. 6(d). Moreover, it is worthwhile to note that 93.8% of initial discharge capacity is able to be well maintained when this full cells are cycled 500 times at the low temperature of −25 °C. In addition, the coulombic efficiencies of approaching 100% are evidenced, which is beneficial for long-term cycling. Such superb electrochemical performances for SIFCs even at the low working temperatures make the as-prepared NVPF-NS cathode material as one of the most promising candidates to realize its practical application in the future.

3 Conclusions

In summary, a novel nano self-assembly process of NVPF was successfully realized based on surface energy adjustment and vanadium site regulation of NVPF by heterovalent Mn^{2+} substitution, and the unique NVPF-NS material with a 2D nanosheet-like structure was prepared. Furthermore, the prepared NVPF-NS acting as cathode material in SIBs can demonstrate significantly enhanced electrochemical performances, including extraordinary C_S (120 mAh·g^{-1} at 0.1 C), remarkable rate capability (85.7 mAh·g^{-1} at 20 C), prominent cycling stability (capacity retention of 80.7% over 1,000 cycles at 1 C), and simultaneously distinguished LT performance (the capacity retention can exceed 93.8% after 500 cycles at 0.5 C and −25 °C). The reason for these improved performances of NVPF-NS is that the unique 2D nanosheet-like structure provides more active sites, enhanced electronic conductivity and ion mobility rate, and stable crystal structure, which are demonstrated convincingly by theoretical and experimental (SEM, XPS, GITT, CV, and *in-situ* XRD) measurement analyses. Accordingly, these findings suggest doping strategy for NASICON-type fluorophosphates is viable to achieve unique morphology control and further electrochemical performance improvement for advanced SIBs with great potential application.

Acknowledgements

We gratefully acknowledge the financial support from the National Natural Science Foundation of China (Nos. 91963118, 52173246, and 52102213), the Science Technology Program of Jilin Province (No. 20200201066JC), and the 111 Project (No. B13013).

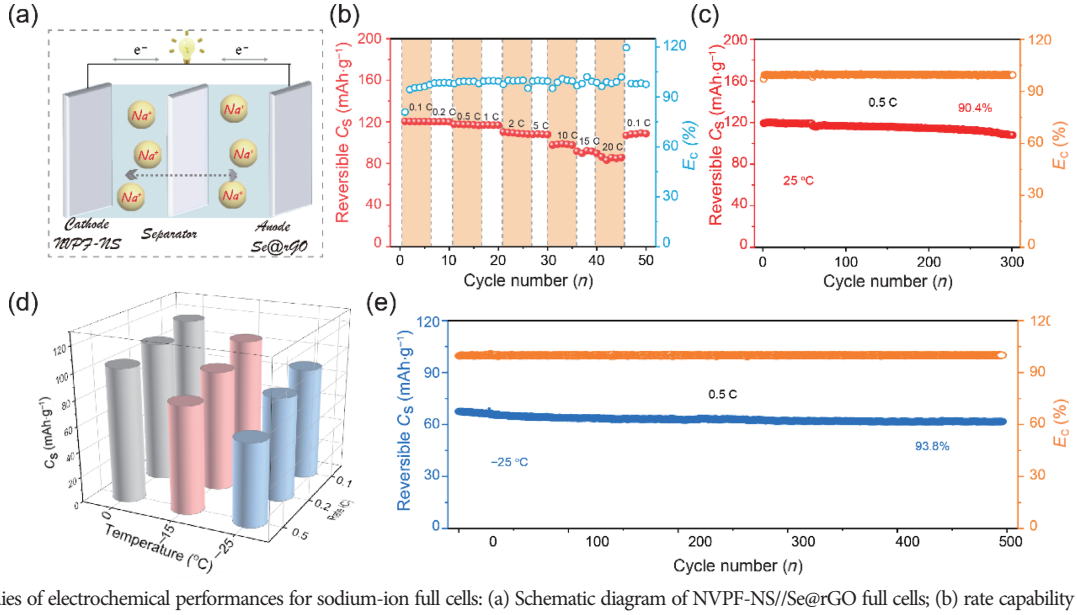

Figure 6 Studies of electrochemical performances for sodium-ion full cells: (a) Schematic diagram of NVPF-NS//Se@rGO full cells; (b) rate capability and (c) cycling performance at room temperature; (d) rate capability and (e) cycling performance at low temperatures.

Electronic Supplementary Material: Supplementary material (experimental section, XRD patterns, FTIR spectrum, TEM image, the full XPS spectra, SEM images, charge/discharge curves, one single GITT profile, the procedure for calculation $D_{app,Na}$, the refined crystallographic data, and ICP result) is available in the online version of this article at https://doi.org/10.1007/s12274-022-4687-6.

References

[1] Delmas, C. Sodium and sodium-ion batteries: 50 years of research. *Adv. Energy Mater.* **2018**, *8*, 1703137.

[2] Tian, Y. S.; Zeng, G. B.; Rutt, A.; Shi, T.; Kim, H.; Wang, J. Y.; Koettgen, J.; Sun, Y. Z.; Ouyang, B.; Chen, T. N. et al. Promises and challenges of next-generation "beyond Li-ion" batteries for electric vehicles and grid decarbonization. *Chem. Rev.* **2021**, *121*, 1623–1669.

[3] Chen, F. H.; Wu, Y. W.; Zhang, H. H.; Long, Z. T.; Lin, X. X.; Chen, M. Z.; Chen, Q.; Luo, Y. F.; Chou, S. L.; Zeng, R. H. The modulation of the discharge plateau of benzoquinone for sodium-ion batteries. *Int. J. Miner. Metall. Mater.* **2021**, *28*, 1675–1683.

[4] Deng, L.; Goh, K.; Yu, F. D.; Xia, Y.; Jiang, Y. S.; Ke, W.; Han, Y.; Que, L. F.; Zhou, J.; Wang, Z. B. Self-optimizing weak solvation effects achieving faster low-temperature charge transfer kinetics for high-voltage $Na_3V_2(PO_4)_2F_3$ cathode. *Energy Stor. Mater.* **2022**, *44*, 82–92.

[5] Ge, P.; Hou, H. S.; Li, S. J.; Huang, L. P.; Ji, X. B. Three-dimensional hierarchical framework assembled by cobblestone-like $CoSe_2$@C nanospheres for ultrastable sodium-ion storage. *ACS Appl. Mater. Interfaces* **2018**, *10*, 14716–14726.

[6] Wei, C.; Fu, X. Y.; Zhang, L. L.; Liu, J.; Sun, P. P.; Gao, L.; Chang, K. J.; Yang, X. L. Structural regulated nickel hexacyanoferrate with superior sodium storage performance by K-doping. *Chem. Eng. J.* **2021**, *421*, 127760.

[7] Yuan, D.; Dou, Y. H.; Tian, Y. H.; Adekoya, D.; Xu, L.; Zhang, S. Q. Robust pseudocapacitive sodium cation intercalation induced by cobalt vacancies at atomically thin $Co_{1-x}Se_2$/graphene heterostructure for sodium-ion batteries. *Angew. Chem., Int. Ed.* **2021**, *60*, 18830–18837.

[8] Gu, E. L.; Liu, S. H.; Zhang, Z. Z.; Fang, Y. Y.; Zhou, X. S.; Bao, J. C. An efficient sodium-ion battery consisting of reduced graphene oxide bonded $Na_3V_2(PO_4)_3$ in a composite carbon network. *J. Alloys Compd.* **2018**, *767*, 131–140.

[9] Gu, Z. Y.; Guo, J. Z.; Zhao, X. X.; Wang, X. T.; Xie, D.; Sun, Z. H.; Zhao, C. D.; Liang, H. J.; Li, W. H.; Wu, X. L. High-ionicity fluorophosphate lattice via aliovalent substitution as advanced cathode materials in sodium-ion batteries. *InfoMat* **2021**, *3*, 694–704.

[10] Shen, L. Y.; Li, Y.; Roy, S.; Yin, X. P.; Liu, W. B.; Shi, S. S.; Wang, X.; Yin, X. M.; Zhang, J. J.; Zhao, Y. F. A robust carbon coating of $Na_3V_2(PO_4)_3$ cathode material for high performance sodium-ion batteries. *Chin. Chem. Lett.* **2021**, *32*, 3570–3574.

[11] Wang, Y. H.; Li, X. T.; Wang, W. P.; Yan, H. J.; Xin, S.; Guo, Y. G. Chalcogen cathode and its conversion electrochemistry in rechargeable Li/Na batteries. *Sci. China Chem.* **2020**, *63*, 1402–1415.

[12] Wu, J. X.; Lin, C.; Liang, Q. H.; Zhou, G. D.; Liu, J. P.; Liang, G. M.; Wang, M.; Li, B. H.; Hu, L.; Ciucci, F. et al. Sodium-rich NASICON-structured cathodes for boosting the energy density and lifespan of sodium-free-anode sodium metal batteries. *InfoMat* **2022**, *4*, e12288.

[13] Xu, J. Y.; Gu, E. L.; Zhang, Z. Z.; Xu, Z. H.; Xu, Y. F.; Du, Y. C.; Zhu, X. S.; Zhou, X. S. Fabrication of porous $Na_3V_2(PO_4)_3$/reduced graphene oxide hollow spheres with enhanced sodium storage performance. *J. Colloid Interface Sci.* **2020**, *567*, 84–91.

[14] Bucher, N.; Hartung, S.; Franklin, J. B.; Wise, A. M.; Lim, L. Y.; Chen, H. Y.; Weker, J. N.; Toney, M. F.; Srinivasan, M. P2-$Na_xCo_yMn_{1-y}O_2$ (y = 0, 0.1) as cathode materials in sodium-ion batteries-effects of doping and morphology to enhance cycling stability. *Chem. Mater.* **2016**, *28*, 2041–2051.

[15] Guhl, C.; Rohrer, J.; Kehne, P.; Ferber, T.; Alff, L.; Albe, K.; Jaegermann, W.; Komissinskiy, P.; Hausbrand, R. The role of covalent bonding and anionic redox for the performance of sodium cobaltate electrode materials. *Energy Stor. Mater.* **2021**, *37*, 190–198.

[16] Liu, Q. N.; Hu, Z.; Li, W. J.; Zou, C.; Jin, H. L.; Wang, S.; Chou, S. L.; Dou, S. X. Sodium transition metal oxides: The preferred cathode choice for future sodium-ion batteries? *Energy Environ. Sci.* **2021**, *14*, 158–179.

[17] Liu, Z. G.; Jiang, K. Z.; Chu, S. Y.; Wu, J. H.; Xu, H.; Zhang, X. P.; Wang, P.; Guo, S. H.; Zhou, H. S. Integrating P2 into O′3 toward a robust Mn-Based layered cathode for sodium-ion batteries. *J. Mater. Chem. A* **2020**, *8*, 23820–23826.

[18] Ortiz-Vitoriano, N.; Drewett, N. E.; Gonzalo, E.; Rojo, T. High performance manganese-based layered oxide cathodes: Overcoming the challenges of sodium ion batteries. *Energy Environ. Sci.* **2017**, *10*, 1051–1074.

[19] Wang, H.; Liao, X. Z.; Yang, Y.; Yan, X. M.; He, Y. S.; Ma, Z. F. Large-scale synthesis of $NaNi_{1/3}Fe_{1/3}Mn_{1/3}O_2$ as high performance cathode materials for sodium ion batteries. *J. Electrochem. Soc.* **2016**, *163*, A565–A570.

[20] Wei, F. L.; Zhang, Q. P.; Zhang, P.; Tian, W. Q.; Dai, K. H.; Zhang, L.; Mao, J.; Shao, G. S. Review-research progress on layered transition metal oxide cathode materials for sodium ion batteries. *J. Electrochem. Soc.* **2021**, *168*, 050524.

[21] Xiao, Y.; Abbasi, N. M.; Zhu, Y. F.; Li, S.; Tan, S. J.; Ling, W.; Peng, L.; Yang, T. Q.; Wang, L. D.; Guo, X. D. et al. Layered oxide cathodes promoted by structure modulation technology for sodium-ion batteries. *Adv. Funct. Mater.* **2020**, *30*, 2001334.

[22] Zhao, C. L.; Ding, F. X.; Lu, Y. X.; Chen, L. Q.; Hu, Y. S. High-entropy layered oxide cathodes for sodium-ion batteries. *Angew. Chem., Int. Ed.* **2020**, *59*, 264–269.

[23] Cao, X. X.; Pan, A. Q.; Yin, B.; Fang, G. Z.; Wang, Y. P.; Kong, X. Z.; Zhu, T.; Zhou, J.; Cao, G. Z.; Liang, S. Q. Nanoflake-constructed porous $Na_3V_2(PO_4)_3$/C hierarchical microspheres as a bicontinuous cathode for sodium-ion batteries applications. *Nano Energy* **2019**, *60*, 312–323.

[24] Cheng, J.; Chen, Y. J.; Sun, S. Q.; Tian, Z. Y.; Linghu, Y. Y.; Tian, Z.; Wang, C.; He, Z. F.; Guo, L. $Na_3V_2(PO_4)_3$/C·$Na_3V_2(PO_4)_2F_3$/C@rGO blended cathode material with elevated energy density for sodium ion batteries. *Ceram. Int.* **2021**, *47*, 18065–18074.

[25] Hou, J. R.; Hadouchi, M.; Sui, L. J.; Liu, J.; Tang, M. X.; Kan, W. H.; Avdeev, M.; Zhong, G. M.; Liao, Y. K.; Lai, Y. H. et al. Unlocking fast and reversible sodium intercalation in NASICON $Na_4MnV(PO_4)_3$ by fluorine substitution. *Energy Stor. Mater.* **2021**, *42*, 307–316.

[26] Jin, T.; Li, H. X.; Zhu, K. J.; Wang, P. F.; Liu, P.; Jiao, L. F. Polyanion-type cathode materials for sodium-ion batteries. *Chem. Soc. Rev.* **2020**, *49*, 2342–2377.

[27] Heng, Y. L.; Gu, Z. Y.; Guo, J. Z.; Wu, X. L. Research progresses on vanadium-based cathode materials for aqueous zinc-ion batteries. *Acta Phys. -Chim. Sin.* **2021**, *37*, 2005013.

[28] Sharma, L.; Adiga, S. P.; Alshareef, H. N.; Barpanda, P. Fluorophosphates: Next generation cathode materials for rechargeable batteries. *Adv. Energy Mater.* **2020**, *10*, 2001449.

[29] Gebert, F.; Cortie, D. L.; Bouwer, J. C.; Wang, W. L.; Yan, Z. C.; Dou, S. X.; Chou, S. L. Epitaxial nickel ferrocyanide stabilizes jahn-teller distortions of manganese ferrocyanide for sodium-ion batteries. *Angew. Chem., Int. Ed.* **2021**, *60*, 18519–18526.

[30] Liu, Q. N.; Hu, Z.; Chen, M. Z.; Zou, C.; Jin, H. L.; Wang, S.; Chou, S. L.; Liu, Y.; Dou, S. X. The cathode choice for commercialization of sodium-ion batteries: Layered transition metal oxides versus prussian blue analogs. *Adv. Funct. Mater.* **2020**, *30*, 1909530.

[31] Peng, J.; Zhang, W.; Wang, J. S.; Li, L.; Lai, W. H.; Yang, Q. R.; Zhang, B. W.; Li, X. N.; Du, Y. M.; Liu, H. W. et al. Processing rusty metals into versatile prussian blue for sustainable energy storage. *Adv. Energy Mater.* **2021**, *11*, 2102356.

[32] Qian, J. F.; Wu, C.; Cao, Y. L.; Ma, Z. F.; Huang, Y. H.; Ai, X. P.; Yang, H. X. Prussian blue cathode materials for sodium-ion batteries and other ion batteries. *Adv. Energy Mater.* **2018**, *8*, 1702619.

[33] Pi, Y. Q.; Gan, Z. W.; Yan, M. Y.; Pei, C. Y.; Yu, H.; Ge, Y. W.;

An, Q. Y.; Mai, L. Q. Insight into pre-sodiation in $Na_3V_2(PO_4)_2F_3$/C@hard carbon full cells for promoting the development of sodium-ion battery. *Chem. Eng. J.* **2021**, *413*, 127565.

[34] Shen, C.; Long, H.; Wang, G. C.; Lu, W.; Shao, L.; Xie, K. Y. $Na_3V_2(PO_4)_2F_3$@C dispersed within carbon nanotube frameworks as a high tap density cathode for high-performance sodium-ion batteries. *J. Mater. Chem. A* **2018**, *6*, 6007–6014.

[35] Zhu, L.; Wang, H.; Sun, D.; Tang, Y. G.; Wang, H. Y. A comprehensive review on the fabrication, modification and applications of $Na_3V_2(PO_4)_2F_3$ cathodes. *J. Mater. Chem. A* **2020**, *8*, 21387–21407.

[36] Li, Y. S.; Liang, X. H.; Chen, G. L.; Zhong, W. T.; Deng, Q.; Zheng, F. H.; Yang, C. H.; Liu, M. L.; Hu, J. H. *In-situ* constructing $Na_3V_2(PO_4)_2F_3$/carbon nanocubes for fast ion diffusion with high-performance Na^+-storage. *Chem. Eng. J.* **2020**, *387*, 123952.

[37] Guo, C.; Yang, J. W.; Cui, Z. Y.; Qi, S.; Peng, Q. Q.; Sun, W. W.; Lv, L. P.; Xu, Y.; Wang, Y.; Chen, S. Q. *In-situ* structural evolution analysis of Zr-doped $Na_3V_2(PO_4)_2F_3$ coated by N-doped carbon layer as high-performance cathode for sodium-ion batteries. *J. Energy Chem.* **2022**, *65*, 514–523.

[38] Li, L.; Xu, Y. L.; Chang, R.; Wang, C.; He, S. N.; Ding, X. D. Unraveling the mechanism of optimal concentration for Fe substitution in $Na_3V_2(PO_4)_2F_3$/C for sodium-ion batteries. *Energy Stor. Mater.* **2021**, *37*, 325–335.

[39] Li, W.; Yao, Z. J.; Zhang, S. Z.; Wang, X. L.; Xia, X. H.; Gu, C. D.; Tu, J. P. High-performance $Na_3V_2(PO_4)_2F_{25}O_{0.5}$ cathode: Hybrid reaction mechanism study via *ex-situ* XRD and sodium storage properties in solid-state batteries. *Chem. Eng. J.* **2021**, *423*, 130310.

[40] Puspitasari, D. A.; Patra, J.; Hung, I. M.; Bresser, D.; Lee, T. C.; Chang, J. K. Optimizing the Mg doping concentration of $Na_3V_{2-x}Mg_x(PO_4)_2F_3$/C for enhanced sodiation/desodiation properties. *ACS Sustainable Chem. Eng.* **2021**, *9*, 6962–6971.

[41] Yi, G. D.; Fan, C. L.; Hu, Z.; Zhang, W. H.; Han, S. C.; Liu, J. S. Construction of high performance *N*-doped $Na_3V_2(PO_4)_2F_3$/C cathode assisting by plasma enhanced chemical vapor deposition for sodium-ion batteries. *Electrochim. Acta* **2021**, *383*, 138370.

[42] Mukherjee, A.; Sharabani, T.; Sharma, R.; Okashy, S.; Noked, M. Effect of crystal structure and morphology on $Na_3V_2(PO_4)_2F_3$ performances for Na-ion batteries. *Batteries Supercaps* **2020**, *3*, 510–518.

[43] Zhao, L. N.; Rong, X. H.; Niu, Y. S.; Xu, R.; Zhang, T.; Li, T.; Yu, Y.; Hou, Y. L. Ostwald ripening tailoring hierarchically porous $Na_3V_2(PO_4)_2O_2F$ hollow nanospheres for superior high-rate and ultrastable sodium ion storage. *Small* **2020**, *16*, 2004925.

[44] Zheng, L. M.; Zhang, D. T.; Wang, X. Y.; Guo, G. S. Continuous-flow rapid and controllable microfluidic synthesis of sodium vanadium fluorophosphate as a cathode material. *Appl. Mater. Today* **2021**, *23*, 101032.

[45] Zhu, W. K.; Liang, K.; Ren, Y. R. Modification of the morphology of $Na_3V_2(PO_4)_2F_3$ as cathode material for sodium-ion batteries by polyvinylpyrrolidone. *Ceram. Int.* **2021**, *47*, 17192–17201.

[46] Li, M. G.; Xia, Z. G.; Huang, Y. R.; Tao, L.; Chao, Y. G.; Yin, K.; Yang, W. X.; Yang, W. W.; Yu, W. S.; Guo, S. J. Rh-doped PdCu ordered intermetallics for enhanced oxygen reduction electrocatalysis with superior methanol tolerance. *Acta Phys. -Chim. Sin.* **2020**, *36*, 1912049.

[47] Li, Z. Y.; Peng, Z. L.; Sun, R.; Qin, Z. X.; Liu, X. L.; Wang, C. H.; Fan, H. S.; Lu, S. J. Super Na^+ half/full batteries and ultrafast Na^+ diffusion kinetics of cobalt-nickel selenide from assembling $Co_{05}Ni_{0.5}Se_2$@NC nanosheets into cross-stacked architecture. *Chin. J. Chem.* **2021**, *39*, 2599–2606.

[48] Li, Z. Y.; Sun, R.; Qin, Z. X.; Liu, X. L.; Wang, C. H.; Lu, S. J.; Zhang, Y. F.; Fan, H. S. Coupling of ReS_2 nanosheet arrays with hollow $NiCoS_4$ nanocubes enables ultrafast Na^+ diffusion kinetics and super Na^+ storage of a $NiCoS_4$@ReS_2 heterostructure. *Mater. Chem. Front.* **2021**, *5*, 7540–7547.

[49] Liao, J. Y.; Chen, C. L.; Hu, Q.; Du, Y. C.; He, Y. N.; Xu, Y. F.; Zhang, Z. Z.; Zhou, X. S. A low-strain phosphate cathode for high-rate and ultralong cycle-life potassium-ion batteries. *Angew. Chem., Int. Ed.* **2021**, *60*, 25575–25582.

[50] Qi, X. R.; Liu, Y.; Ma, L. L.; Hou, B. X.; Zhang, H. W.; Li, X. H.; Wang, Y. S.; Hui, Y. Q.; Wang, R. X.; Bai, C. Y. et al. Delicate synthesis of quasi-inverse opal structural $Na_3V_2(PO_4)_3$/N-C and $Na_4MnV(PO_4)_3$/N-C as cathode for high-rate sodium-ion batteries. *Rare Met.* **2022**, *41*, 1637–1646.

[51] Zhu, H. Y.; Li, Z. Y.; Xu, F.; Qin, Z. X.; Sun, R.; Wang, C. H.; Lu, S. J.; Zhang, Y. F.; Fan, H. S. Ni_3Se_4@$CoSe_2$ hetero-nanocrystals encapsulated into CNT-porous carbon interpenetrating frameworks for high-performance sodium ion battery. *J. Colloid Interface Sci.* **2022**, *611*, 718–725.

[52] Criado, A.; Lavela, P.; Ortiz, G.; Tirado, J. L.; Pérez-Vicente, C.; Bahrou, N.; Edfouf, Z. Highly dispersed oleic-induced nanometric C@$Na_3V_2(PO_4)_2F_3$ composites for efficient Na-ion batteries. *Electrochim. Acta* **2020**, *332*, 135502.

[53] Qi, Y. R.; Mu, L. Q.; Zhao, J. M.; Hu, Y. S.; Liu, H. Z.; Dai, S. pH-regulative synthesis of $Na_3(VPO_4)_2F_3$ nanoflowers and their improved Na cycling stability. *J. Mater. Chem. A* **2016**, *4*, 7178–7184.

[54] Ji, X.; Li, H. J.; Wu, Z. G.; Cheng, S.; Hu, H. R.; Yan, D.; Zhuo, R. F.; Wang, J.; Yan, P. X. Growth of AlN hexagonal oriented complex nanostructures induced by nucleus arrangement. *CrystEngComm* **2011**, *13*, 5198–5203.

[55] Tanta, R.; Kanne, T.; Amaduzzi, F.; Liao, Z. Y.; Madsen, M. H.; Alarcón-Lladó, E.; Krogstrup, P.; Johnson, E.; Morral, A. F.; Vosch, T. et al. Morphology and composition of oxidized InAs nanowires studied by combined Raman spectroscopy and transmission electron microscopy. *Nanotechnology* **2016**, *27*, 305704.

[56] Xia, W. W.; Xu, F.; Zhu, C. Y.; Xin, H. L.; Xu, Q. Y.; Sun, P. P.; Sun, L. T. Probing microstructure and phase evolution of α-MoO_3 nanobelts for sodium-ion batteries by *in situ* transmission electron microscopy. *Nano Energy* **2016**, *27*, 447–456.

[57] Song, W. X.; Cao, X. Y.; Wu, Z. P.; Chen, J.; Zhu, Y. R.; Hou, H. S.; Lan, Q.; Ji, X. B. Investigation of the sodium ion pathway and cathode behavior in $Na_3V_2(PO_4)_2F_3$ combined via a first principles calculation. *Langmuir* **2014**, *30*, 12438–12446.

[58] Wang, M. X.; Wang, K.; Huang, X. B.; Zhou, T.; Xie, H. S.; Ren, Y. R. Improved sodium storage properties of Zr-doped $Na_3V_2(PO_4)_2F_3$/C as cathode material for sodium ion batteries. *Ceram. Int.* **2020**, *46*, 28490–28498.

[59] Li, Q.; Rellán-Piñeiro, M.; Almora-Barrios, N.; Garcia-Ratés, M.; Remediakis, I. N.; López, N. Shape control in concave metal nanoparticles by etching. *Nanoscale* **2017**, *9*, 13089–13094.

[60] Yi, H. M.; Lin, L.; Ling, M. X.; Lv, Z. Q.; Li, R.; Fu, Q.; Zhang, H. M.; Zheng, Q.; Li, X. F. Scalable and economic synthesis of high-performance $Na_3V_2(PO_4)_2F_3$ by a solvothermal-ball-milling method. *ACS Energy Lett.* **2019**, *4*, 1565–1571.

[61] Broux, T.; Bamine, T.; Fauth, F.; Simonelli, L.; Olszewski, W.; Marini, C.; Ménétrier, M.; Carlier, D.; Masquelier, C.; Croguennec, L. Strong impact of the oxygen content in $Na_3V_2(PO_4)_2F_{3-y}O_y$ ($0 \le y \le 0.5$) on its structural and electrochemical properties. *Chem. Mater.* **2016**, *28*, 7683–7692.

[62] Broux, T.; Fleutot, B.; David, R.; Brüll, A.; Veber, P.; Fauth, F.; Courty, M.; Croguennec, L.; Masquelier, C. Temperature dependence of structural and transport properties for $Na_3V_2(PO_4)_2F_3$ and $Na_3V_2(PO_4)_2F_{2.5}O_{0.5}$. *Chem. Mater.* **2018**, *30*, 358–365.

[63] Iarchuk, A. R.; Sheptyakov, D. V.; Abakumov, A. M. Hydrothermal microwave-assisted synthesis of $Na_{3+x}V_{2-y}Mn_y(PO_4)_2F_3$ solid solutions as potential positive electrodes for Na-ion batteries. *ACS Appl. Energy Mater.* **2021**, *4*, 5007–5014.

[64] Zheng, Q.; Ni, X.; Lin, L.; Yi, H. M.; Han, X. W.; Li, X. F.; Bao, X. H.; Zhang, H. M. Towards enhanced sodium storage by investigation of the Li ion doping and rearrangement mechanism in $Na_3V_2(PO_4)_3$ for sodium ion batteries. *J. Mater. Chem. A* **2018**, *6*, 4209–4218.

[65] Zhang, Z. B.; Chen, Z. H.; Mai, Z. X.; Peng, K. Y.; Deng, Q. L.; Bayaguud, A.; Zhao, P. F.; Fu, Y. P.; Yu, Y.; Zhu, C. B. Toward high power-high energy sodium cathodes: A case study of bicontinuous ordered network of 3D porous $Na_3(VO)_2(PO_4)_2F$/rGO with pseudocapacitance effect. *Small* **2019**, *15*, 1900356.

[66] Liu, H. D.; Wang, J.; Zhang, X. F.; Zhou, D.; Qi, X.; Qiu, B.; Fang, J. H.; Kloepsch, R.; Schumacher, G.; Liu, Z. P. et al. Morphological evolution of high-voltage spinel $LiNi_{0.5}Mn_{1.5}O_4$ cathode materials for

lithium-ion batteries: The critical effects of surface orientations and particle size. *ACS Appl. Mater. Interfaces* **2016**, *8*, 4661–4675.

[67] Wang, Y. Y.; Hou, B. H.; Guo, J. Z.; Ning, Q. L.; Pang, W. L.; Wang, J. W.; Lü, C. L.; Wu, X. L. An ultralong lifespan and low-temperature workable sodium-ion full battery for stationary energy storage. *Adv. Energy Mater.* **2018**, *8*, 1703252.

[68] Gu, Z. Y.; Guo, J. Z.; Sun, Z. H.; Zhao, X. X.; Li, W. H.; Yang, X.; Liang, H. J.; Zhao, C. D.; Wu, X. L. Carbon-coating-increased working voltage and energy density towards an advanced $Na_3V_2(PO_4)_2F_3$@C cathode in sodium-ion batteries. *Sci. Bull.* **2020**, *65*, 702–710.

[69] Gu, Z. Y.; Guo, J. Z.; Sun, Z. H.; Zhao, X. X.; Wang, X. T.; Liang, H. J.; Zhao, B.; Li, W. H.; Pan, X. M.; Wu, X. L. Aliovalent-ion-induced lattice regulation based on charge balance theory: Advanced fluorophosphate cathode for sodium-ion full batteries. *Small* **2021**, *17*, 2102010.

[70] Hwang, J.; Takeuchi, K.; Matsumoto, K.; Hagiwara, R. NASICON vs. Na metal: A new counter electrode to evaluate electrodes for Na secondary batteries. *J. Mater. Chem. A* **2019**, *7*, 27057–27065.

[71] Li, C. C.; Zhang, X. S.; Zhu, Y. H.; Zhang, Y.; Xin, S.; Wan, L. J.; Guo, Y. G. Modulating the lithiophilicity at electrode/electrolyte interface for high-energy Li-metal batteries. *Energy Mater.* **2021**, *1*, 100017.